Use of a virtual wall valve in polydimethylsiloxane microfluidic devices for bioanalytical applications

Hsuan-Hong Lai,[1] Wei Xu,[1] and Nancy L. Allbritton[1,2,a)]
[1]*Department of Chemistry, University of North Carolina, Chapel Hill, North Carolina 27599, USA*
[2]*Department of Biomedical Engineering, University of North Carolina, Chapel Hill, North Carolina 27599, USA and North Carolina State University, Raleigh, North Carolina 27695, USA*

(Received 21 January 2011; accepted 12 April 2011; published online 5 May 2011)

A simple method for micromanipulation of liquids and/or small groups of cells is presented in this study. Microfabricated sieving structures composed of PDMS (polydimethylsiloxane) were used to segregate aqueous solutions. This microfluidic valving scheme was an application of Cassie–Baxter wetting and was termed "virtual walls" as a nonsolid barrier exists at an air/water interface. The manipulation of the virtual-air-wall valve was accomplished by controlling the strength of surface-tension and hydrostatic-pressure forces. Virtual walls with a range of feature sizes were designed and characterized by monitoring air and water displacement in response to hydrostatic pressure. Thresholds for the virtual-air-wall valves to be turned on or off were quantified. The walls could also be formed or dissipated by the focused microbeam of a pulsed laser. As an illustration of the virtual wall utility, a series of microfluidic applications were demonstrated. First, the capability of virtual walls to temporarily segregate liquids was integrated into a device utilized to establish a chemical gradient. In a second application, the arraying of nonadherent cells within individual aqueous cavities created by the virtual walls was demonstrated. Individual cells were also released from the cavities on demand using a focused microbeam. The virtual walls were simple and easy-to-fabricate without the requirement for surface treatment or precision alignment, and should find usage in bioanalytical applications. © *2011 American Institute of Physics.*
[doi:10.1063/1.3584848]

I. INTRODUCTION

Microfluidic devices have been widely employed for biochemical and bioanalytical assays. Many of these applications rely on the integration of multiple functions into a single chip.[1,2] Integrating multiple discrete aqueous, organic, or air phases into a fluidic network for reaction or mixing is an example. Separating these phases is typically via partitioning or diffusion and often requires the control and maintenance of nonsolid interfaces.[3] Earlier work frequently depended on laminar fluid flow and the precise tuning of flow rates between the miscible phases.[4,5] Because of its dynamic nature, this interface is vulnerable to perturbations and can be difficult to manipulate. Surface coatings have also been used to create a relatively well-controlled and stable air:liquid interface, termed virtual walls.[6] Several applications have employed virtual walls, for example, interfacial polymerization,[7,8] gaseous phase/liquid phase reactions,[6,9] or nanoliter liquid metering.[10] The method relies on the positioning or patterning of a nonsolid barrier by modification of surface energy, typically the hydrophobicity/hydrophilicity of a surface.

[a)]Author to whom correspondence should be addressed. Electronic mail: nlallbri@unc.edu. FAX: 919-966-2291, 919-962-2388.

By far the most common techniques for the formation of virtual walls are patterned self-assembled monolayers,[8,10–12] microplasma jet writing,[13] and sol-gel inkjet printing,[14] applied to surfaces such as silicon,[10] glass,[6,9] or plastic.[14] These methods can precisely define the spatial location of the virtual walls. However, device fabrication using these methods can be tedious and typically involves precision alignment. In addition, the flow paths defined by the surface modification are usually vulnerable to strong hydrodynamic forces.[11] An alternative strategy developed by Xu *et al.* in PDMS (polydimethylsiloxane) microchannels eliminates the need for surface patterning, functionalization, or precision alignment.[15] In this method, PDMS microcavities produced Cassie–Baxter wetting yielding a hybrid air:PDMS wall in a microchannel.[16,17] This virtual wall design provided improved resistance to hydrodynamic forces which is particularly important for applications that require microfluidic manipulation using pressurized fluid flow. This feature suggests that these walls might also be a good candidate for use as a valve. Compared with current designs of microvalves, for example, electric,[18] piezoelectric,[19] magnetic,[20] and thermal,[21] a virtual wall valve would be easily fabricated as well as simple in use.

In the current study, hybrid air:PDMS walls were evaluated for their ability to function as a valve actuated through the use of hydrodynamic pressure. The walls were formed by fabricating a one-dimensional array of PDMS posts between two microchannels. The influence of hydrodynamic pressure and PDMS post size and spacing on the hybrid wall stability and valving action was theoretically and experimentally examined. Usage of the pressure-controllable virtual walls was then demonstrated in microfluidic and bioanalytical applications. These included segregation of liquids with subsequent gradient formation. Finally, a one-dimensional, releasable array of cells was demonstrated within aqueous cavities created by the hybrid walls.

II. EXPERIMENTAL SECTION

A. Materials

1002F-50 photoresist was prepared in the laboratory by mixing bisphenol A epoxy resin (EPON™ resin 1002F, CAS# 25036–25–3, Miller-Stephenson Chemical Co. Inc., Sylmar, CA), photoacid generator (Cyracure™ photoinitiator UVI-6976, CAS# 109037–75–4, Dow Chemical, Torrance, CA), and organic solvent, GBL (γ-Butyrolactone, CAS# 96–48–0, Sigma-Aldrich, St. Louis, MO), at the ratios described previously.[22] PDMS (Sylgard 184) was purchased from Dow Corning, Midland, MI. The perfluoroalkyl silane, (heptadecafluoro-1,1,2,2-tetrahydrodecyl) trichlorosilane, was obtained from Gelest Inc., Morrisville, PA. Precleaned microscope sides ($75\times38\times1$ mm) were obtained from Fisher Scientific, Pittsburgh, PA. Silicon wafers were purchased from WaferNet Inc., San Jose, CA. Chrome photomasks were fabricated by Fineline Imaging, Colorado Springs, CO, with a resolution of $>50,800$ dpi. Oregon Green 488 and fluorescein were purchased from Invitrogen Corp., Carlsbad, CA. All other reagents were purchased from Sigma-Aldrich, St. Louis, MO.

B. Fabrication of master molds using 1002F photoresist

A silicon wafer was precleaned by air-plasma treatment (plasma cleaner, model# PDC-001, Harrick Plasma, Ithaca, NY) for 25 min and then immediately spin-coated with 1002F-50 photoresist.[22] A photoresist film was spin-coated on the silicon wafer by using a spin coater (WS-400B-6NPP-Lite spin processor, Laurell Technologies Corp., North Wales, PA) operating at 500 rpm for 13 s, followed by 1300 rpm for 30 s. The coated silicon wafer then proceeded to a two-step soft-bake process at a temperature of 65 °C for 30 min followed by 95 °C for 60 min. A refractive index matching liquid ($n_D=1.6020$, Cargille-Sacher Laboratories Inc., Cedar Grove, NJ) was placed between the photomask and 1002F film during UV exposure to increase the fidelity of lithographic printing. The 1002F film was exposed to 900 mJ/cm^2 (Oriel Flood Exposure Source, model # 97435, equipped with a 500 W mercury lamp, Newport Corp., Irvine, CA). The wafer then received a postexposure bake (65 °C for 1 min followed by 95 °C for 10 min). The photoresist films were developed in propylene glycol monomethyl ether acetate for 9 min, rinsed with isopropyl alcohol, and dried with a nitrogen stream. An additional bake (hard bake)

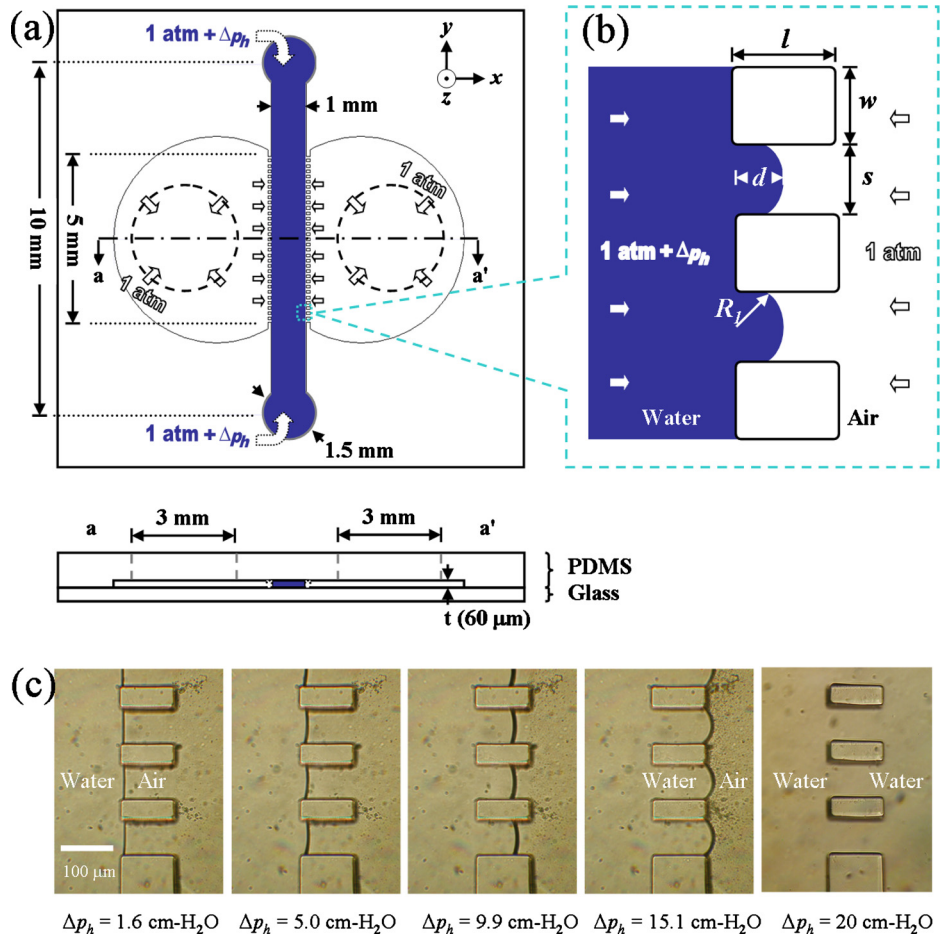

FIG. 1. A virtual wall microfluidic device. (a) The planar view and side view of the virtual wall chamber. (b) A magnified view of the micropost array. (c) Transmitted light images of the air/water interface under influence of hydrostatic pressure. The micropost feature sizes were $l=125$, $w=50$, and $s=75$ μm.

was applied to the films by placing them at 130 °C for 50 min to complete cross-linking. The surface of the 1002F master was silanized via a vapor-phase reaction with perfluoroalkyl silane as described previously.[23]

C. Fabrication of PDMS:glass microdevices

The microfluidic device was fabricated using a micromolded PDMS top piece and a microscope slide as the bottom. The PDMS piece with imprinted chambers and channel was fabricated through vulcanization of Sylgard 184 on a master mold as previously described.[24] The total thickness of the PDMS piece was 5 mm. The central channel in the center of the device was 10 mm in length and 1 mm in width [Fig. 1(a)]. Two circular regions (6 mm in diameter) were formed on either side of the central channel. The length of the junction between the circular areas and the straight channel was 5 mm. Along the 5 mm junction, rectangular PDMS posts were periodically spaced. Access ports or holes (1.5 mm diameter) were punched through the PDMS piece at the termini of the central channel. Access ports to the two circular regions on either side of the central channel were 3 mm in diameter. Before the PDMS top piece was bound to a precleaned microscope slide, the PDMS piece and glass slide were cleaned with 75% ethanol and acetone, respectively. The PDMS and glass pieces were dried in a nitrogen stream and baked at 80 °C for 10 min. To permanently bond the PDMS top and glass bottom, both pieces were oxidized (Harrick plasma cleaner) for 45 s and then mated. The sealed device was baked at 80 °C in air for 1 week to permit

hydrophobic recovery of the PDMS piece.[25] The depth of the microfluidic channel (or height of the posts) in the final device was determined by confocal microscopy to be 60 μm.

D. Measurement of the displacement and curvature of the virtual walls

The displacement (d) of the air:water interface between the PDMS posts [Fig. 1(b)] was recorded using a digital camera and an inverted microscope (Eclipse TE300, Nikon Instruments Inc., Melville, NY). The pressure difference (Δp_h) was the difference in the hydrostatic pressure between the reservoirs of the central channel and the reservoirs of the circular side regions [Fig. 1(a)]. A maximum or critical pressure difference, Δp_c, was defined as that Δp_h in which fluid from the central channel entered through the gaps in the PDMS posts and escaped into the either of the adjacent circular reservoirs. The Δp_h was recorded in the units of cm-H_2O and each data point represented the average value of at least three measurements.

The curvature at the air:water interface was measured by 3D (three-dimensional) imaging using a confocal microscope (Zeiss 510 Meta Laser Scanning Confocal Microscope, Carl Zeiss MicroImaging Inc., Thornwood, NY). 3.3 ppm of fluorescein was added to the water loaded into the central channel to enhance imaging of the air:water meniscus. The radii were calculated by fitting the interface surface to a circle.

E. Cell culture

BA/F3 cells (mouse leukemia) were cultured at 37 °C in a humidified 5% CO_2 atmosphere in RPMI 1640 supplemented with 10% fetal bovine serum. Penicillin (100 units/ml) and streptomycin (100 μg/ml) were added to the media to inhibit bacterial growth. In the microfluidic device, unless stated otherwise, BA/F3 cells were incubated in ECB (135 mM NaCl, 5 mM KCl, 10 mM HEPES at pH 7.4, 1 mM $MgCl_2$, 1 mM $CaCl_2$, and 10 mM glucose), as described previously.[24]

F. Microscopy and optical delivery system for pulsed laser

Images of cells were captured using an analog or monochrome CCD camera (Photometrics CoolSNAP *fx*, Roper Scientific Inc., Tucson, AZ) through a bright-field objective lens (40X, N.A. 0.80, Zeiss Achroplan) in an inverted microscope (Carl Zeiss MicroImaging Inc., Thornwood, NY). METAFLUOR software (Molecular Devices Corp., Downingtown, PA) was used to collect the images. A frequency-doubled Q-switched Nd:YAG laser (neodymium-doped yttrium aluminum garnet laser) (5 ns, 532 nm, Continuum Inc., Santa Clara, CA) was steered into the rear port of the microscope as described previously.[24] A 15/85 beamsplitter in the beam path was used to send a small portion of the beam energy to an energy meter (EPM1000, Coherent Inc., Santa Clara, CA).

III. RESULTS AND DISCUSSION

A. Manipulation of virtual walls by pressure

A PDMS microfluidic device with a glass bottom was used to examine the formation and stability of hybrid air:PDMS walls [Fig. 1(a)]. This hybrid device was utilized due to its simple fabrication and the high quality, optical window provided by the glass bottom. This last feature enables access to the channel with a tightly focused laser microbeam.[24] The device was composed of a straight channel with adjacent circular reservoirs on either side of the channel. The central channel was separated from each circular region by an array of rectangular microposts arranged parallel to the channel. The feature sizes of each micropost, l and w, and the gap between the post, s, are depicted in Fig. 1(b). The height (t) of the post was always constant at 60 μm. When air was introduced into the two circular reservoirs and water loaded through the central channel, air was trapped between the PDMS posts due to the hydrophobicity of the PDMS. The surface of the air:water interface was nearly flat. As a hydrodynamic force (Δp_h) was applied to the central fluid-filled channel, the curvature of the air:water interface increased and the interface advanced from the intersection of the post with the water-filled channel toward the air-filled reservoirs [Fig. 1(c)]. As Δp_h was decreased, the interface retreated. However, when Δp_h was sufficiently large

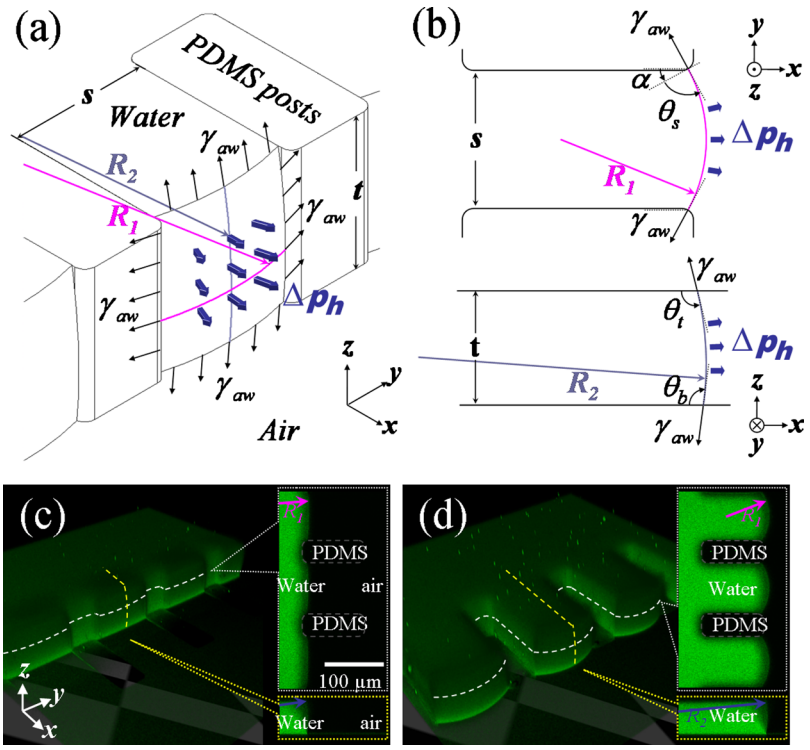

FIG. 2. (a) Schematic illustration of the micropost array and water menisci bulging out through the gap of the posts under the influence of surface tension and hydrostatic pressure. The curvatures of the meniscoid surface were defined as depicted. (b) The planar views of (a) in x-y plane and x-z plane, showing the balance of the forces acting on the air:water interface. [(c) and (d)] Confocal microscopy 3D imaging of the pressurized water menisci guided in the microstructures between the PDMS posts. The feature sizes of the microfabricated structures are $l=120$ μm, $w=45$ μm, and $s=90$ μm. ($t=60$ μm). (c) and (d) are the 3D analysis of the menisci under the Δp_h, 5.3 and 11.8 cm-H_2O, respectively. The insets are the cross sections of the 3D analysis in x-y plane and x-z plane. 3.3 ppm fluorescein was added to water to enhance the contrast and appeared green in the images.

[for example, $\Delta p_h > 20$ cm-H_2O for the design shown in Fig. 1(c)], water was able to penetrate between the PDMS posts into the circular reservoirs and the virtual walls were lost. The walls could only be regenerated by removing all fluid from the device followed by reintroduction of water into main channel under a low Δp_h.

Virtual walls can be utilized to segregate liquids while release of the walls under hydrostatic pressure can act to combine liquids. To precisely control the actuation of this virtual wall valve, a better understanding of the mechanisms involving the evolution and dissipation of the wall by pressure was required. The interfacial tension at the solid:liquid:gas interface between the posts provided the force to oppose Δp_h [Figs. 2(a) and 2(b)]. Below a critical Δp_h, an equilibrium between the opposing forces of surface tension and pressure was attained. As Δp_h increased, the degree of the curvature of the interface increased accordingly. To monitor the change in the shape of the air:water interface between the PDMS posts, the interface was imaged by confocal microscopy at different z and an image of the interface was reconstructed [Figs. 2(c) and 2(d)]. The radii of curvature R_1 and R_2 were defined as shown in Fig. 2(b). The reconstructed images displayed two prominent features: R_1 was nearly independent of z and R_2 was very large so that the shape of the air:water interface surface was nearly cylindrical. These features suggested that the forces due to surface tension and pressure acted predominantly along the x axis. This may be due to the use of the glass base in the device. The forces at the air:water interface are governed by the Young–Laplace[26] equation (see the supplementary materials),

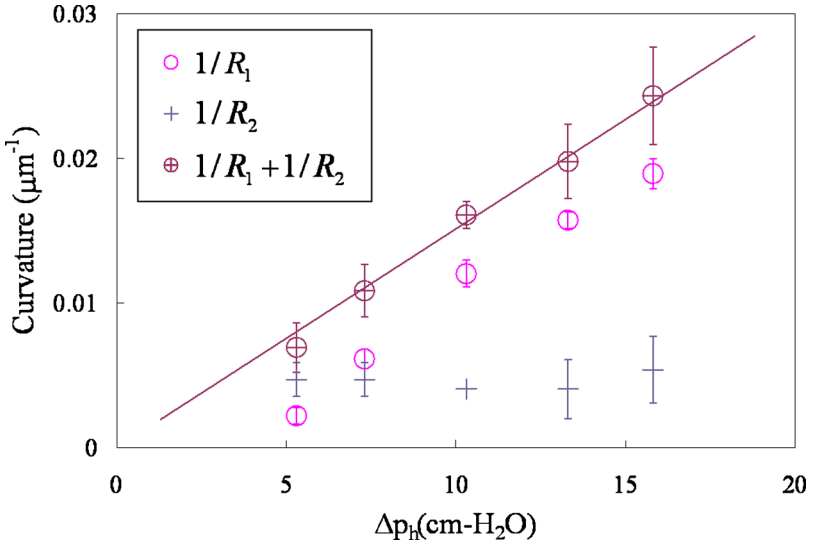

FIG. 3. Fitting the curvatures measured from the 3D analysis into the Young–Laplace equation. R_1 and R_2 were defined as per Figs. 2(a) and 2(b).

$$\Delta p_h = \gamma_{aw}\left[\frac{1}{R_1}+\frac{1}{R_2}\right], \tag{1}$$

where Δp_h was opposed by the force of the surface tension which depended on the curvature of the air:water interface. The curvature in turn was achieved primarily via transmission of the pressure through the contact angles of the water with the PDMS surface. To determine how the walls of the hybrid device influenced the curvature of the air:water surface, R_1 and R_2 were measured by fitting the interface in the confocal images to a circle. $1/R_1$ and $1/R_2$ were then plotted against Δp_h (Fig. 3). When Δp_h was high ($\Delta p_h > 6$ cm-H_2O), $1/R_1$ played a dominant role in the surface tension. In contrast when Δp_h was low ($\Delta p_h < 6$ cm-H_2O), $1/R_2$ dominated the surface tension forces. For this hybrid glass:PDMS device, R_2 was largely independent of Δp_h (Fig. 3).

B. Influence of the feature sizes on the virtual walls

To understand how the PDMS post design impacted the virtual walls, devices with varying l, w, and s were fabricated (Fig. 1). For these studies, a dimensionless term, d/l, was used as a variable where d is the distance that the air:water interface is displaced within the PDMS posts. d was measured from the center of the air:water interface to the inlet of the PDMS posts [Fig. 1(b)]. d/l was recorded for different Δp_h. d/l versus Δp_h was measured for varying l, w, and s. The dependence of d/l on Δp_h was independent of l and w (data not shown). The shape of the d/l versus Δp_h curve was similar at different s with d/l undergoing a rapid transition moving between 0 and 1 at a transition pressure Δp_t [Fig. 4(a)]. The location or Δp_t of the sharp transition in d/l was related to s, the distance between the posts. At large s (90–185 μm), the sharp d/l transition occurred at a low Δp_t of 8–9 cm-H_2O, whereas a much greater applied pressure (13–18 cm-H_2O) was required for the d/l transition for a small s (35–55 μm). The steep change of d/l with respect to Δp_h at the transition stage occurred when the forces due to hydropressure exceeded that due to the surface tension, so the air:water interface advanced rapidly along the length of the PDMS post. Not surprisingly, a greater force or pressure was required to force the water through the smaller channels between the more tightly spaced posts.

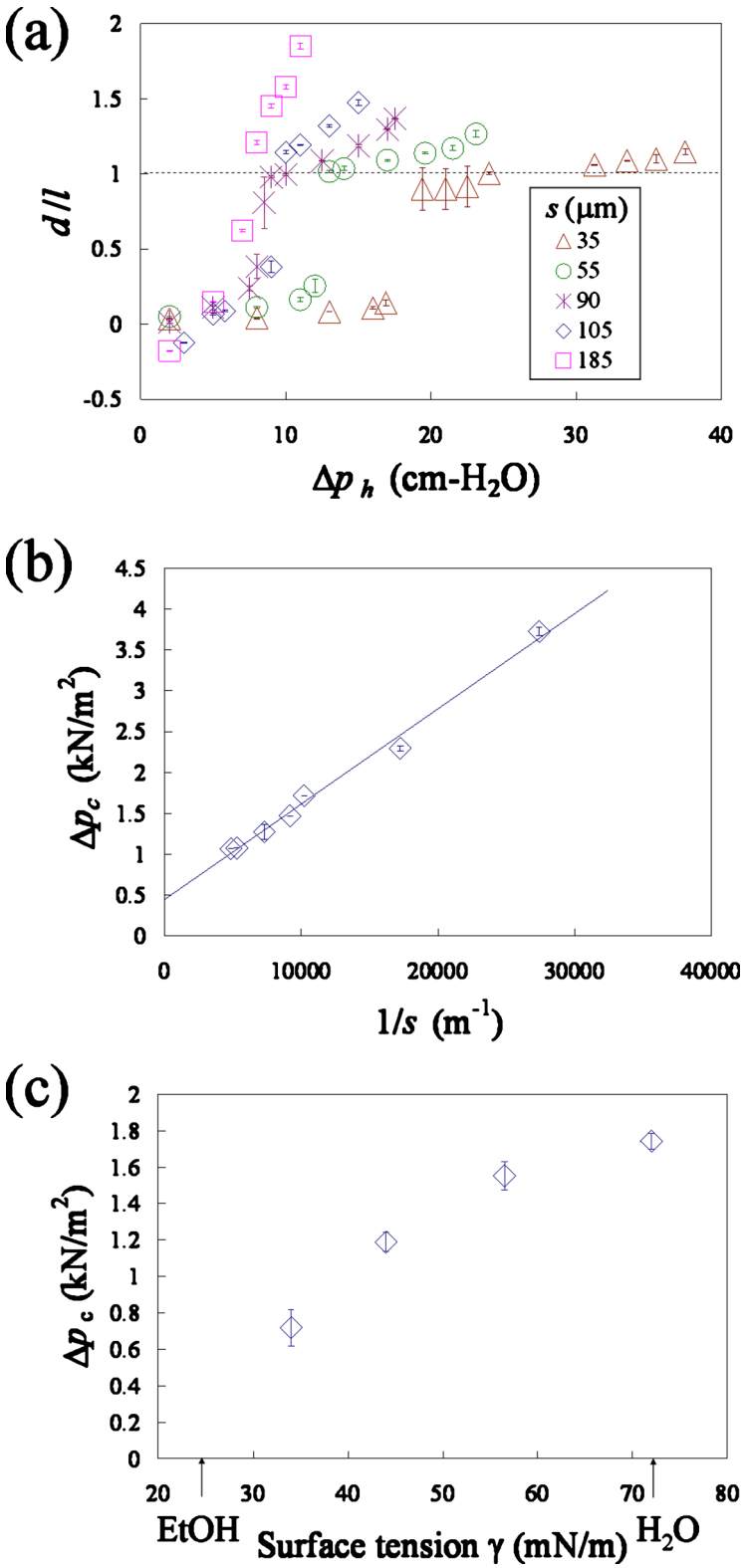

FIG. 4. (a) d/l was plotted against Δp_h with respect to the feature sizes s, where l and w remained constant (l=90 and w=45). (b) Linear regression of Δp_c with respect to $1/s$. (c) The graph of Δp_c with respect to surface tension of the ethanol/water mixture. The virtual wall chamber used in this examination had a gap of 90 μm.

C. Influence of the feature sizes on the critical pressure (Δp_c)

The critical pressure (Δp_c) was defined as the Δp_h required to break the virtual wall or force water from the central channel between the posts and into the adjacent reservoir. Δp_c corresponds to the maximum surface-tension force that can be exerted at the air:water interface. Δp_c was independent of w and l but highly dependent on s (Fig. S1 in the supplementary materials). Typical values of Δp_c ranged from 10 to 40 cm-H_2O, which is at least twice that of surface-directed virtual walls.[6] For large s (>100 μm), Δp_c approached a value of 10 cm-H_2O. While at small s (35 μm), the air wall was very stable with a Δp_c of 40 cm-H_2O. Δp_c was inversely proportional to s. This relationship is readily understood from Eq. (S9).[26] The maximal theoretical surface tension force would be achieved at an $\alpha+\theta_s$ of 180°, where $(\alpha+\theta_s)$ is the angle between the surface tension vector and the x axis, as depicted in the top planar view in Fig. 2(b). θ_s is the contact angle of water with the PDMS sidewall. In practice, however, $(\alpha+\theta_s)=180°$ is never achieved but rather the walls fail at a critical α (α_c) that yields a value of less than 180° for $(\alpha+\theta_s)$. At this α_c, Δp_h is equal to Δp_c and can be expressed as

$$\Delta p_c = A\frac{1}{s} + B, \tag{2}$$

where A and B are the slope and intercept and defined as

$$A = -2\gamma_{aw}\cos(\alpha_c + \theta_s), \tag{3}$$

$$B = -\frac{\gamma_{aw}}{t}(\cos(\theta_t) + \cos(\theta_b)). \tag{4}$$

Thus, Δp_c possesses a linear dependence on s^{-1} [Fig. 4(b)]. When the experimentally measured Δp_c versus s^{-1} curve was fitted to a straight line, the R-squared value was 0.99 (R, the Pearson product-moment correlation coefficient[27]) and the best-fit constants A and B are 117 mN/m and 446 N/m^2, respectively. Utilizing γ_{aw} (72 mN/m for water)[28] and θ_s (109° obtained from confocal image data, Figs. 2(c) and 2(d)), α_c was 35° [Eq. (3)]. The calculated α_c was similar to that observed in the experiments. The experimentally measured t, θ_t, and θ_b were used to calculate a B value of 417 N/m^2 similar to that predicted above. Thus, the behaviors of the virtual walls in this hybrid glass:PDMS device when manipulated by hydrodynamic pressure are well predicted. This feature enables the virtual walls to be formed or dissipated on demand for use in microfluidic devices.

D. Influence of surface tension on the adhesion of virtual walls

In order to achieve formation of virtual walls by Cassie–Baxter wetting, the choice of the liquid is critical. The liquid:solid interfacial tension must be greater than the solid material's surface energy in the presence of air.[17] This requirement implies that the contact angle of the liquid on the solid surface should be greater than 90° in order to form Cassie–Baxter wetting, i.e., $\Delta p_c > 0$.[28] Thus, manipulation of the liquid:solid interfacial tension or liquid contact angle on the solid might be an effective way to tailor the performance of the virtual wall valve. To manipulate the interfacial tension, ethanol was mixed in varying ratios with water.[29] The ethanol/water mixture was then used to form virtual walls in the PDMS device. As expected, the critical pressure Δp_c was reduced as the content of ethanol was increased or surface tension decreased [Fig. 4(c)]. The highest concentration of ethanol aqueous solution we used to achieve virtual walls was 40 wt % and the corresponding Δp_c was 7.9 cm (0.72 kN/m^2). Higher concentrations of ethanol resulted in fragmented and unstable virtual walls.

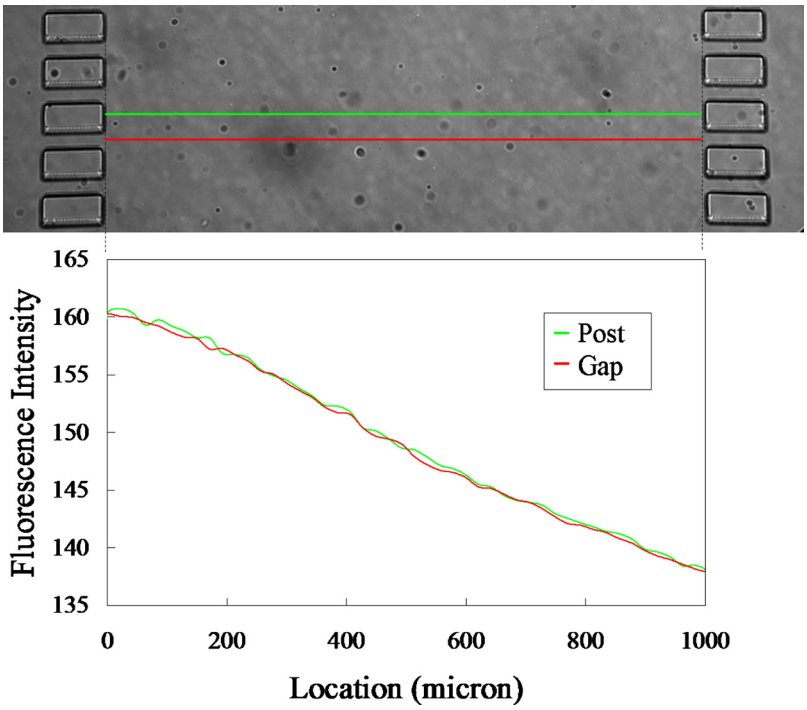

FIG. 5. Use of the virtual walls to initiate formation of a chemical gradient across the central channel. The upper panel is a brightfield image of the device. Oregon Green 488 (3 μM in ECB) was loaded into the left reservoir. ECB alone was loaded into the right reservoir. Application of pressure to the reservoirs displaced the virtual walls. The line traces in the image indicate where the fluorescence intensity profiles were measured. The specifications of the device are identical to those in Fig. 1(a). The width of the central channel was 1 mm and the feature sizes for the microposts were l=90 μm, w=45 μm, and s=35 μm. The lower panel shows the fluorescence along the lines depicted.

E. Formation of a concentration gradient in the presence of the virtual-wall posts

Microfluidic devices have been widely utilized for cell biology applications. A key application for microdevices has been the development of microfluidic chambers for application of chemical gradients to biological and chemical reaction systems.[30,31] Despite these advances, conventional gradient-generators, such as the Zigmond chamber,[32] are still widely used for studying cell chemotaxis. This is largely due to the complexity in the operation of the microscale devices. Thus, there is still a need for simple-and-easy-to-use chemical gradient devices for biomedical applications. The virtual walls may permit formation of a gradient across the central channel on demand by dissipation of the virtual walls between the two outer chambers. To determine whether a linear gradient could be formed across the central channel, a fluorescent dye solution (3 μM Oregon Green 488 in ECB) was introduced in one reservoir of the device in Fig. 1(a), while the opposite reservoir was filled with only ECB. During buffer loading Δp_h was maintained below Δp_t. The gradient was initiated after flowing a solution through the central channel at Δp_h greater than Δp_c. The fluorescence across the channel was then measured over time. A linear concentration gradient was established after 50 min (Fig. 5) and was stable for at least 15 h. The concentration gradient was identical irrespective of whether the fluorescence was measured across the channel between two posts or between two gaps; thus the presence of the posts did not disrupt gradient formation. These data suggest that the virtual walls could act as a successful component of a chemotactic device with removal of the walls used as a mechanism to establish the gradient.

F. Use virtual walls for cell trapping

Cell arrays have been achieved by techniques such as microwell arrays[33–36] and cell trap/docking arrays.[37–40] With most of these methods, cells are generally not retrieved or are retrieved

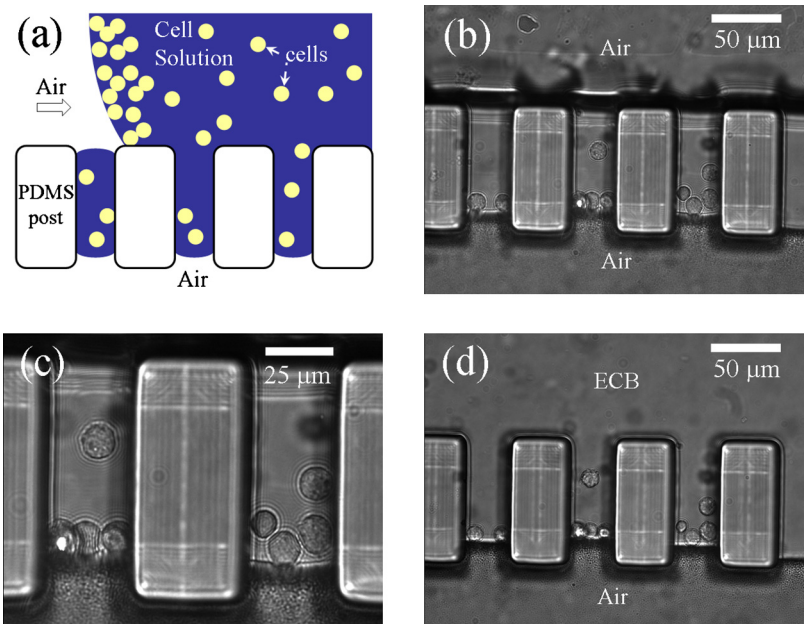

FIG. 6. (a) A schematic drawing showing the use of a virtual wall chamber for cell trapping. (b) BA/F3 cells were loaded into the gaps between PDMS posts by flowing them through the central channel. The fluid in the main channel was replaced with air leaving the cells and fluid trapped within the posts. The dimensions of the micropost array were $l=90$, $w=45$, and $s=35$ μm. (c) is the closeup view of (b). (d) The cells remained in place when the air was removed and additional aqueous buffers passed through the central channel.

mixed together as a bulk population.[37,39,40] Single nonadherent cells have been removed from an array of microtraps with a manually controlled pipette[33] or by the optical pressure of a laser beam.[35] Since these methods are either slow due to the inability to automate or require the use of a potentially cell-damaging, high-powered light source, additional strategies to array and release single cells would be of value to the biomedical community. Arrays of virtual walls have the potential to entrap and display cells. Further, since the virtual walls can be readily manipulated or removed, the virtual wall traps may be competent to release cells on demand. To assess the ability of the arrayed microcavities to display cells, cells loaded through the main device channel. The cells entered into the cavities between the posts formed by the air walls. A slightly lower pressure ($\Delta p_h < \Delta p_t$) was used to transport the cells through the length of the main channel followed by a larger pressure ($\Delta p_t < \Delta p_h < \Delta p_c$) to drive the cell into the cavities. A well controlled pressure protocol ensured that cells were distributed evenly into the cavity arrays (Fig. 6).

Once the cells were loaded into the cavities, the excess cell solution in the main channel was removed and air filled into the channel leaving the cells arrayed in the space between the posts [Fig. 6(a)–6(c)]. To gain access to the trapped cells, the main channel was refilled with ECB which merged with the fluid between the posts [Fig. 6(d)]. Removal and refilling of air or aqueous solutions from the main channel did not disturb the cells. The cells could also be loaded with fluorescent dyes and other reagents while in the linear array of cavities by washing dye-loaded fluids in and out of the central channel (Fig. 7). While cells were easily accessed for microscopic analysis, retrieval of single cells could not be accomplished by simply washing fluid through the main channel. It was desirable to retrieve single cells from the surface-tension created cavities so that cells of interest could be cultured for later biochemical analysis. To retrieve a cell of interest, a laser microbeam was focused into an adjacent PDMS post resulting in degassing of the PDMS post and formation of an air bubble in the microcavity adjacent to the post (Fig. 8). The cell of interest was then expelled from the cavity by the gas bubble and captured by flowing buffer through the central channel.

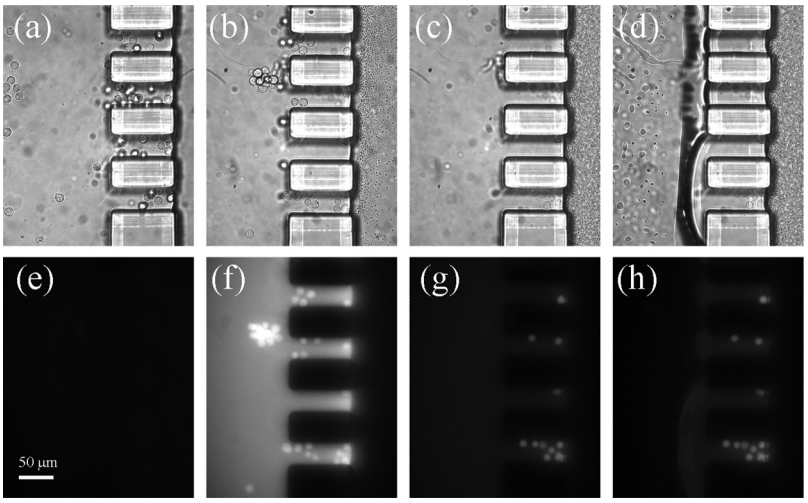

FIG. 7. Demonstration of fluorescence labeling of BA/F3 cells arrayed between the posts. (a) Cells were initially loaded into the gaps between the posts while in their growth medium. In the image an aqueous solution is present between the posts and to the left of the array, while air is present on the right side of the array. (b) The growth medium was sequentially replaced with air and then aqueous buffer with 30 μM Oregon Green 488 carboxylic acid diacetate introduced into the main channel. In the image the Oregon Green-containing solution is present between the posts and to the left of the array, while air is present on the right side of the array. (c) The dye solution was sequentially replaced with air and then dye-free aqueous buffer. In the image the aqueous buffer is present between the posts and to the left of the array, while air is present on the right side of the array. (d) The aqueous buffer in the main channel has been replaced with air. (e), (f), (g), and (h) are fluorescence images corresponding to (a), (b), (c), and (d), respectively. The dimensions of the micropost array were l=90, w=45, and s=35 μm.

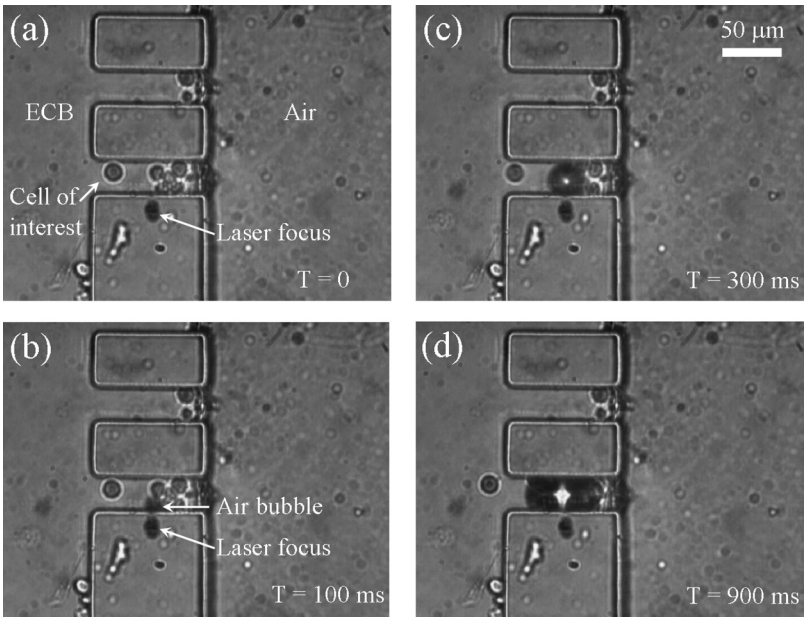

FIG. 8. Bright-field images showing cell retrieval with a focused microbeam. (a) Time zero showing the cell of interest and the position of the focused microbeam. (b) Delivery of the first pulse initiated the formation of a small air bubble. (c) After three pulses were delivered, the size of bubble increased rapidly moving the cell outward toward the main channel. (d) The cell was expelled from the gap after nine laser pulses were delivered. The dimensions of the micropost array were l=90, w=45, and s=35 μm. The laser pulse energy was 3 μJ/pulse (5 ns pulse duration, 532 nm).

G. Laser-based actuation of virtual wall valves

The virtual walls could be removed or formed by appropriate application of a pulsed laser. The microchip design was identical to that in Fig. 1(a). When the air:fluid interface was intact, creation of a plasma was used to disrupt the air:water interface and eliminate the air wall [Fig. S2(a) in the supplementary materials]. A Nd:YAG laser pulse (8 μJ) was focused in the fluid between two microposts and adjacent to the air:water interface. The focused microbeam in the liquid created a plasma which in turn produced a cavitation bubble and shock wave. If of sufficient magnitude, the resultant local increase in pressure overcame surface tension resulting in the localized removal of the barrier. Due to the hydrophilic nature of the glass base, the liquid flowed through this breach into the opposing side chamber. As the flowing liquid filled the opposing side chamber, the removable air barrier was disrupted along its entire length [Fig. S2(b) in the supplementary materials]. Thus, laser-based breach at the wall between a two posts led to the collapse of the entire virtual wall.

When the gaps between posts were filled with water, the focused microbeam could be used to form air bubbles between the posts regenerating the virtual wall. Repeated focused laser pulses (10 μJ) were delivered into the liquid between two posts. When of sufficient intensity and number (>10), the laser pulses generated a cavitation bubble with residual bubbles remaining in the liquid and merging with subsequent bubbles to form a single large bubble. This final bubble was of sufficient size to regenerate the gas:liquid interface between the two microposts [Fig. S2(c) in the supplementary materials]. Thus, the virtual walls could also be reformed using a focused microbeam.

IV. CONCLUSIONS

In this study, we investigated the properties of a virtual wall valve by monitoring the interfacial curvature changes and particularly the location of the meniscus relative to the post length to understand the effects of pressure and quantify air wall rupture. The effects of the feature sizes for virtual walls as well as the surface tension were also examined. We demonstrated that virtual walls are compatible with common fluidic features such as chemical gradients or cell arrays. An advantage of the virtual walls is that they can be utilized as a highly controllable valve without the need for surface coatings, multilayered fabrication, or movable mechanical components. Thus, simplicity plus the ability to control valve behavior by understanding surface tension principles are key advantages of the virtual walls. These simple structures should find wide use in practical fluidic biosystems.

ACKNOWLEDGMENTS

This research was supported by NIH Grant Nos. EB004436 and CA139599. The authors thank Dr. Christopher E. Sims and Dr. Yuli Wang for advice on cell culture, Dr. Michael Chua in the Michael Hooker Microscopy Facility for assistance with confocal microscopy, Dr. Rahul Dhopeshwarkar for consultation on modeling, and Emily Johnson for fabrication of the virtual wall device.

[1] P. Abgrall and A. M. Gue, J. Micromech. Microeng. **17**, R15 (2007).
[2] C. Q. Yi, C. W. Li, S. L. Ji, and M. S. Yang, Anal. Chim. Acta **560**, 1 (2006).
[3] J. Atencia and D. J. Beebe, Nature (London) **437**, 648 (2005).
[4] T. Maruyama, J. Uchida, T. Ohkawa, T. Futami, K. Katayama, K. Nishizawa, K. Sotowa, F. Kubota, N. Kamiyaa, and M. Goto, Lab Chip **3**, 308 (2003).
[5] K. Ueno, F. Kitagawa, and N. Kitamura, Lab Chip **2**, 231 (2002).
[6] B. Zhao, J. S. Moore, and D. J. Beebe, Science **291**, 1023 (2001).
[7] B. Zhao, N. O. L. Viernes, J. S. Moore, and D. J. Beebe, J. Am. Chem. Soc. **124**, 5284 (2002).
[8] D. M. Cheng, Y. J. P. Choe, and H. R. Jiang, J. Microelectromech. Syst. **17**, 962 (2008).
[9] A. Hibara, S. Iwayama, S. Matsuoka, M. Ueno, Y. Kikutani, M. Tokeshi, and T. Kitamori, Anal. Chem. **77**, 943 (2005).
[10] K. Handique, D. T. Burke, C. H. Mastrangelo, and M. A. Burns, Anal. Chem. **72**, 4100 (2000).
[11] B. Zhao, J. S. Moore, and D. J. Beebe, Anal. Chem. **74**, 4259 (2002).
[12] A. Hibara, M. Nonaka, H. Hisamoto, K. Uchiyama, Y. Kikutani, M. Tokeshi, and T. Kitamori, Anal. Chem. **74**, 1724 (2002).

[13] J. West, A. Michels, S. Kittel, P. Jacob, and J. Franzke, Lab Chip **7**, 981 (2007).
[14] P. Lam, K. J. Wynne, and G. E. Wnek, Langmuir **18**, 948 (2002).
[15] W. Xu, "Virtual wall and its applications in microfluidics," Ph.D. dissertation, University of California, Irvine, 2006.
[16] A. Lafuma and D. Quere, Nature Mater. **2**, 457 (2003).
[17] A. B. D. Cassie and S. Baxter, Trans. Faraday Soc. **40**, 546 (1944).
[18] L. Yobas, M. A. Huff, F. J. Lisy, and D. M. Durand, J. Microelectromech. Syst. **10**, 187 (2001).
[19] J. Peirs, D. Reynaerts, and H. Van Brussel, Sens. Actuators, A **85**, 409 (2000).
[20] H. J. Cho, K. W. Oh, C. H. Ahn, P. Boolchand, and T. C. Nam, IEEE Trans. Magn. **37**, 2749 (2001).
[21] H. Takao, K. Miyamura, H. Ebi, M. Ashiki, K. Sawada, and M. Ishida, Sens. Actuators, A **119**, 468 (2005).
[22] J. H. Pai, Y. Wang, G. T. Salazar, C. E. Sims, M. Bachman, G. P. Li, and N. L. Allbritton, Anal. Chem. **79**, 8774 (2007).
[23] Y. L. Wang, C. E. Sims, P. Marc, M. Bachman, G. P. Li, and N. L. Allbritton, Langmuir **22**, 8257 (2006).
[24] H. H. Lai, P. A. Quinto-Su, C. E. Sims, M. Bachman, G. P. Li, V. Venugopalan, and N. L. Allbritton, J. R. Soc., Interface **5**, S113 (2008).
[25] I. J. Chen and E. Lindner, Langmuir **23**, 3118 (2007).
[26] See supplementary material at http://dx.doi.org/10.1063/1.3584848 for derivation of the equations for virtual air walls.
[27] *Encyclopedia of Measurement and Statistics*, edited by N. J. Salkind (SAGE, Thousand Oaks, CA, 2007).
[28] A. W. Adamson and A. P. Gast, *Physical Chemistry of Surfaces*, 6th ed. (Wiley, New York, 1997).
[29] J. H. Sung, K. Park, and D. Kim, J. Phys. Chem. B **109**, 18507 (2005).
[30] S. Kim, H. J. Kim, and N. L. Jeon, Integr. Comp. Biol. **2**, 584 (2010).
[31] D. B. Weibel and G. M. Whitesides, Curr. Opin. Chem. Biol. **10**, 584 (2006).
[32] S. H. Zigmond, J. Cell Biol. **75**, 606 (1977).
[33] S. Yamamura, H. Kishi, Y. Tokimitsu, S. Kondo, R. Honda, S. R. Rao, M. Omori, E. Tamiya, and A. Muraguchi, Anal. Chem. **77**, 8050 (2005).
[34] J. R. Rettig and A. Folch, Anal. Chem. **77**, 5628 (2005).
[35] J. R. Kovac and J. Voldman, Anal. Chem. **79**, 9321 (2007).
[36] M. C. Park, J. Y. Hur, K. W. Kwon, S. H. Park, and K. Y. Suh, Lab Chip **6**, 988 (2006).
[37] S. J. Tan, L. Yobas, G. Y. H. Lee, C. N. Ong, and C. T. Lim, Biomed. Microdevices **11**, 883 (2009).
[38] W. H. Tan and S. Takeuchi, Proc. Natl. Acad. Sci. U.S.A. **104**, 1146 (2007).
[39] D. Di Carlo, L. Y. Wu, and L. P. Lee, Lab Chip **6**, 1445 (2006).
[40] D. Di Carlo, N. Aghdam, and L. P. Lee, Anal. Chem. **78**, 4925 (2006).